Materials Science & Engineering A 817 (2021) 141391

Contents lists available at ScienceDirect

Materials Science & Engineering A

journal homepage: www.elsevier.com/locate/msea

On the probabilistic nature of high-pressure die casting

Ewan Lordan [a,*], Yijie Zhang [a], Kun Dou [a,b], Alain Jacot [a,c], Chrysoula Tzileroglou [a], Paul Blake [d], Zhongyun Fan [a]

[a] Brunel Centre for Advanced Solidification Technology, Brunel University London, Uxbridge, Middlesex, UB83PH, UK
[b] School of Metallurgy and Environment, Central South University, Changsha, 410083, Hunan, China
[c] Calcom ESI SA, Switzerland
[d] Jaguar Land Rover Ltd, Coventry, CV3 4LF, UK

ARTICLE INFO

Keywords:
Al alloys
Casting
X-ray tomography
Defects
Mechanical properties

ABSTRACT

This article unmasks the probabilistic nature of high-pressure die casting; specifically, the cause of scatter in the tensile ductility of die-cast Al8Si0·4Mn0·3Mg (wt.%) alloy. Scatter in tensile ductility is related to the size of large pores and non-metallic inclusions. We propose that these non-metallic inclusions form during the pyrolysis of commercial plunger lubricants, and that these large pores derive from dilatational strains introduced during semi-solid deformation. The apparent randomness of pore formation is thus ascribed to the heterogeneous nature of the semi-solid network. Reducing heat loss in the shot chamber is shown to promote a more homogeneous grain structure, leading to a decrease in the maximum pore size from 1.32 mm to 0.37 mm, and an increase in the minimum tensile ductility from 6.8% to 9.4%.

1. Introduction

High-pressure die casting (HPDC) is widely used in the manufacture of light alloy structures intended for use in automobiles and aeroplanes, due in part to its high dimensional accuracy and suitability for robotic automation. HPDC is characterised by the high-speed injection of molten metal into a sealed mould cavity, followed by solidification under an applied pressure of 30 ~ 100 MPa [1]. The process thus elicits an array of rich and complex phenomena including fluid turbulence, solidification, and semi-solid deformation. Combined, these phenomena make HPDC somewhat probabilistic in nature: the tensile ductility of die-castings is notoriously inconsistent [2–4]. This inconsistency leads to high scrap rates, and increased safety factors for component design. Although the tensile ductility of die-castings has been linked to various casting defects—porosity [5–8], oxides [8,9], and sludge intermetallic particles [9–11] to name a few—the underlying cause of variability remains enigmatic.

Previous investigations into the reliability of die-castings have generally pursued one of three lines of inquiry. The first derives empirical correlations between the tensile ductility and various measures of microstructural uniformity (e.g. bulk porosity content [3,4,12,13], maximum pore size [5–7], grain size [13–15], eutectic fraction [3,4,10]). The second relates the scatter in tensile ductility to statistical variations in melt quality (e.g. chemical composition [11,16], gas content [8], number of inclusions in the melt [9]). The third considers the stochastic nature of fluid flow, and the subsequent encapsulation of air and oxides [17–20]. Although porosity is a recurrent theme in these studies, its formation mechanism is widely disputed [4,9,13]. Tian et al. [9] relate the amount of porosity to the number of inclusions in the melt. Li et al. [13] observe a linear correlation between the volume fraction of porosity and the fraction of primary α-Al_1 grains solidified in the shot chamber. Dong et al. [4] found that the use of vacuum can lead to fewer pores and improved tensile properties. However, these studies assume that porosity is the main source of scatter in tensile ductility. In light of such findings, it would be interesting to determine whether or not this assumption is valid.

Previously [21,22] we simulated the HPDC process using the finite element method (FEM) under the ProCAST (ESI Group) software platform; an optimum plunger speed profile was derived in Ref. [22] based on predictions from the model. Here, we perform HPDC experiments under both *Baseline* and *Optimized* conditions to identify the primary source of scatter in tensile ductility. Based on our findings, we explain the seemingly random nature of pore formation in the HPDC process.

* Corresponding author.
E-mail addresses: ewan.lordan2@brunel.ac.uk, ewan-lordan@live.co.uk (E. Lordan).

https://doi.org/10.1016/j.msea.2021.141391
Received 19 January 2021; Received in revised form 18 March 2021; Accepted 29 April 2021
Available online 4 May 2021

2. Experimental

We begin by defining a set of casting parameters and operating conditions that are representative of commercial foundry practice (see Appendix). This article does not concern the state of the art, but rather aims to reproduce the variability encountered in industry. The established process was used to produce roughly 100 tensile specimens; the mechanical properties of these specimens will serve as a *baseline* for later benchmarking. A similar number of specimens were also produced under *Optimized* conditions, as will be discussed later.

2.1. Casting procedure

Al8Si0·4Mn0·3Mg (wt.%) alloy (40 kg per crucible) was melted in an electric resistance furnace and held at 750 °C for 30 min to maintain a uniform composition distribution. The melt was degassed using a conventional rotary degassing unit for 10 min with a stirring speed of 350 rpm and an argon flow rate of 4 l/min. Although other, more effective, techniques are available (e.g. intensive shearing [8] and ultrasonic processing [23]) rotary degassing was selected as it is most representative of commercial foundry practice. After degassing, the liquid was manually ladled into the shot chamber of a FRECH 4500 kN locking force cold chamber HPDC machine to produce ASTM standard E8/E8M tensile specimens [24]. The die geometry used in this work is shown in Fig. 1. The pouring temperature was maintained at 680 ± 5 °C using a thermocouple. The temperature of the die and shot chamber were held at roughly 200 °C and 180 °C, respectively.

2.2. Casting parameters

Fig. 2 shows the plunger speed profiles considered in this work. Notable differences lie in the speeds attained at displacements of 50 mm and 375 mm (Baseline {0.2 ms^{-1}, 0.3 ms^{-1}} and Optimized {0.4 ms^{-1}, 0.6 ms^{-1}}, respectively). The Baseline profile was defined according to recommendations from the supplier of the HPDC machine (FRECH). Previously [21,22], we simulated the HPDC process using a FEM model developed under the ProCAST software platform. An optimal plunger speed profile (Fig. 2) was derived in Ref. [22] based on the amount and distribution of oxides, entrapped air, and shrinkage porosity predicted by the model. A fast shot speed of 3.6 ms^{-1} was used for both plunger speed profiles based on preliminary trials. A pressure of 32 MPa was selected for the intensification stage, corresponding to the maximum attainable pressure of the hydraulic actuator.

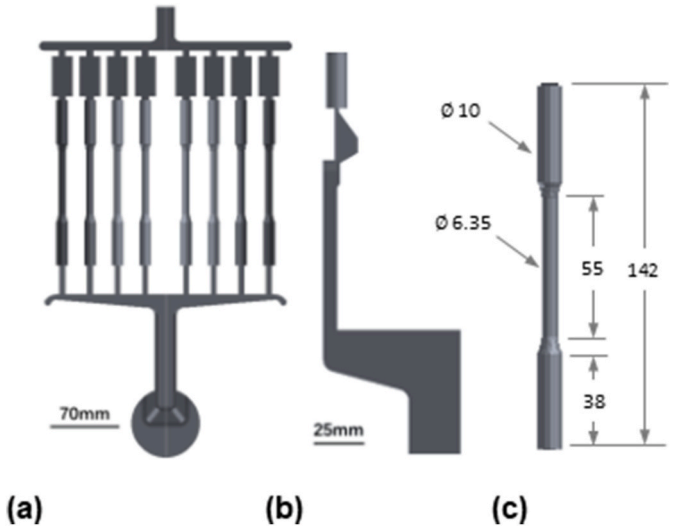

Fig. 1. Die geometry used to produce ASTM standard E8/E8M tensile specimens [24]. (a) Front view. (b) Side view of runner-orifice system. (c) Schematic of tensile specimens (all dimensions in mm).

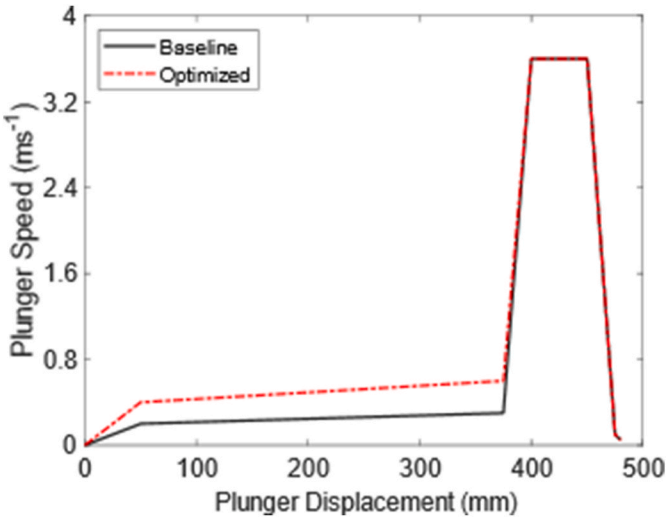

Fig. 2. Baseline and Optimized plunger speed profiles.

2.3. Tensile testing and SEM fractography

Tensile tests were performed at room temperature using an Instron 5500 universal electromechanical testing system equipped with a 50 kN load cell, in accordance with ASTM standard E8/E8M [24]. A schematic of the tensile specimen is shown in Fig. 1(c). Tensile data was acquired using a 50 mm extensometer with a ramp rate of 1 mm/min. Roughly 100 tensile specimens were tested for each plunger speed profile. After fracture, specimens representing the distribution of tensile ductility (with particular emphasis on the lower tail) were isolated and the fracture surfaces examined using a LEO 1450VP SEM (Carl Zeiss AG) equipped with energy dispersive X-ray spectroscopy (EDX).

2.4. X-ray tomography

X-ray tomography was performed using an Xradia 410 Versa (Carl Zeiss AG) microtomography system operated with an accelerating voltage of 80 kV and a power of 10 W. An isotropic voxel was defined with a characteristic length of 3.4 μm. The VGSTUDIO MAX (Volume Graphics GmbH) software was used to perform quantitative analyses on the three-dimensional volumes. An iterative surface determination was performed to isolate the material volume while compensating for local fluctuations in grey value. The VGDEFX module (Volume Graphics GmbH) was used to characterise pores contained in the material, with a minimum pore volume of 8 voxels used in the analysis. Pore size was evaluated using the maximum Feret diameter method (the distance between two parallel tangential planes enclosing the largest dimension of the particle or void). Future reference to particle size will also imply use of the maximum Feret diameter method, with the diameter denoted by D. Preliminary trials revealed that the effects of damage accumulation on pore size and morphology may be ignored due to the brittle nature of fracture. As the average pore sizes (∼ 50 μm) considered in this work are much larger than the voxel size of 3.4 μm, we may safely ignore the effect of image resolution on pore size measurements.

2.5. Electron backscatter diffraction mapping

Samples for electron backscatter diffraction (EBSD) mapping were prepared to a 0.04 μm finish using standard metallurgical techniques. The samples were then polished for 40 min using a vibrational plate, operated at a frequency of 90 Hz. EBSD was carried out on a Crossbeam 350 FIB-SEM (Carl Zeiss AG) equipped with an EDAX EBSD analyser

(EDAX Inc.). EBSD data was acquired at 20 kV with a sample tilt of 70°. Mapping was performed using the TEAM Software package (EDAX Inc.), for which a 152 × 120 μm region was analysed with a step size of 0.4 μm; this step size ensures a minimum of 6 pixels per grain width. After mapping, EBSD data was analysed in the OIM Analysis software (EDAX Inc.).

3. Results

3.1. Mechanical properties

Fig. 3 shows the tensile properties of specimens produced under Baseline and Optimized conditions; 95% confidence ellipses are shown for two-dimensional normally distributed data. Average values and standard deviations are provided in Table 1. The average values and standard deviations are unchanged by the change in plunger speed profile. However, Fig. 3 shows that the variability in tensile strength and tensile ductility is greatly reduced under Optimized conditions (that is, if we define variability as significant *negative* deviations from the average property). For example, minimum values of 6.8% and 9.4% are obtained for the ductility of specimens produced under Baseline and Optimized conditions, respectively. A similar trend is also observed for tensile strength, with minimum values of 275 MPa and 282 MPa reported for the Baseline and Optimized conditions, respectively. The contrary is observed for 0.2% proof strength, with minimum values of 143 MPa and 136 MPa obtained for the Baseline and Optimized conditions, respectively.

3.2. Porosity

From each group, the tensile specimen with the lowest ductility was isolated for further examination; X-ray tomography was used to characterise pores contained in these two specimens. In Fig. 4, the sphericity of each pore is plotted against its maximum Feret diameter (D). Here, sphericity refers to the ratio A_s/A_d where A_d is the surface area of the defect, and A_s is the surface area of a sphere with equivalent volume. Values of sphericity lie between zero and unity, with small values indicative of irregular morphology. Average values for pore size and sphericity are provided in Table 2. The average values and standard deviations are unchanged by the change in plunger kinematics. However, the maximum pore size decreases from 1.32 mm to 0.37 mm following the change from Baseline to Optimized. The irregular morphology (low sphericity) of these pores suggests that they do not originate from the expansion of gaseous phases [3–8].

3.3. Inclusions

Fig. 5(a) shows the largest pore (D=1.32 mm) observed on the fracture surface of the lowest ductility specimen in the Baseline group. Large non-metallic inclusions can be seen within the pore; oxides are also observed in the vicinity of these inclusions. Pores are known to

Table 1
Average tensile properties and standard deviations for samples produced under Baseline and Optimized conditions. Roughly 100 specimens were tested for each condition.

	0.2% Proof strength (MPa)	Tensile strength (MPa)	Tensile ductility (%)
Baseline	148 ± 3 (min. 143)	292 ± 4 (min. 275)	11.6 ± 1.5 (min. 6.8)
Optimized	144 ± 3 (min. 136)	294 ± 4 (min. 282)	11.9 ± 1.4 (min. 9.4)

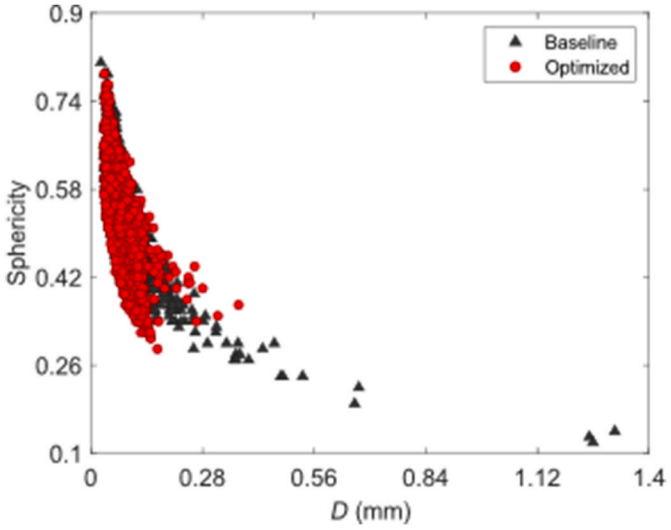

Fig. 4. Pore sphericity vs. maximum Feret diameter (D), for pores identified in the lowest ductility specimens produced under Baseline and Optimized conditions.

Table 2
Average size and sphericity of pores identified in the lowest ductility specimen for the Baseline and Optimized groups.

	Avg. Pore size (mm)	Avg. Sphericity
Baseline	0.05 ± 0.02 (max. 1.32)	0.61 ± 0.07 (min. 0.12)
Optimized	0.05 ± 0.01 (max. 0.37)	0.59 ± 0.07 (min. 0.29)

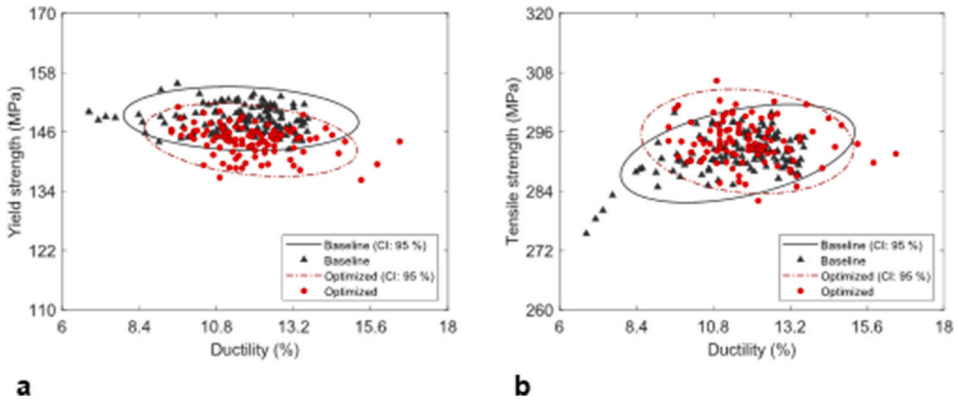

Fig. 3. Tensile properties of specimens produced under Baseline and Optimized conditions. 95% confidence ellipses are shown for two-dimensional normally distributed data (CI: 95%). (a) 0.2% proof stress vs. tensile ductility. (b) Tensile strength vs. tensile ductility.

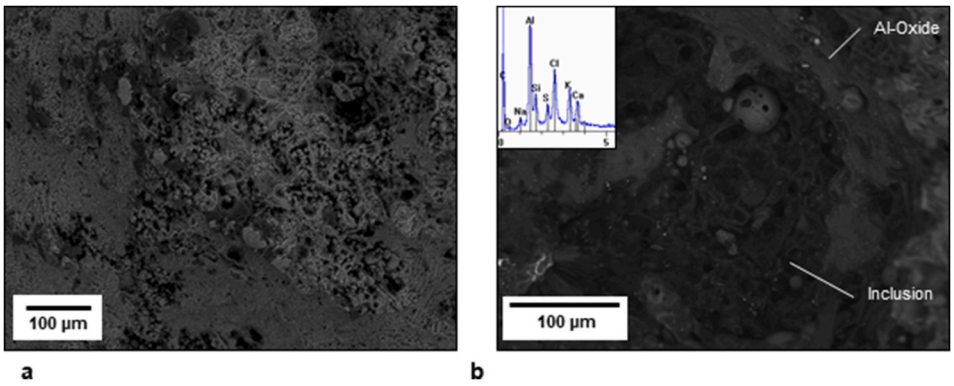

Fig. 5. Representative micrographs of defects observed on the fracture surface of tensile specimens. (a) Pore identified on the lowest ductility Baseline specimen. (b) Non-metallic inclusion; the inset in (b) shows a representative EDX spectrum for such an inclusion. Both images were obtained by detecting backscattered electrons in the SEM. Note that the scale differs in (a) and (b).

nucleate on non-wetted interfaces [25]. Favourable nuclei include the non-wetted surfaces of oxide bifilms and non-metallic inclusions, particularly those comprising low-surface-tension liquids and non-wetted solids [25]. These inclusions, or the accompanying oxides, may act as nuclei for the pores observed in these specimens. Though inclusions in the lowest ductility specimens are relatively small, large non-metallic inclusions (0.4 ∼ 0.7 mm) were observed on the fracture surface of other specimens with a tensile ductility in the range of 8 ∼ 12%. A representative micrograph of such an inclusion is shown in Fig. 5 (b).

3.4. Grain structure

Fig. 6(a and b) shows inverse pole figure (IPF) maps for the Baseline and Optimized samples, produced via EBSD mapping. The grain structure is shown to comprise a mixture of large dendritic primary α-Al_1 grains (30 ∼ 150 µm) solidified in the shot chamber, and smaller globular-rosette primary α-Al_2 grains (∼ 10 µm) formed in the die cavity. Such differences in size and morphology are due to the lower cooling rates (∼ 10 Ks^{-1} [14]) in the shot chamber compared to those in the die cavity (500 ∼ 1000 Ks^{-1} [14]). Additional information regarding the nature of primary α-Al_1 grains and primary α-Al_2 grains can be found in Refs. [14,27]. Increasing the plunger speed from Baseline to Optimized induces a refinement of both large primary α-Al_1 grains and smaller primary α-Al_2 grains, which can be ascribed to reduced heat loss in the shot chamber. Fig. 6(c and d) show grain size distributions corresponding to the IPF maps in Fig. 6(a and b). Grain size distributions are often observed to approximate a lognormal shape, a phenomenon that has previously been attributed to the time-dependent kinetics of crystal growth processes [26]. Accordingly, we present grain size in terms of its

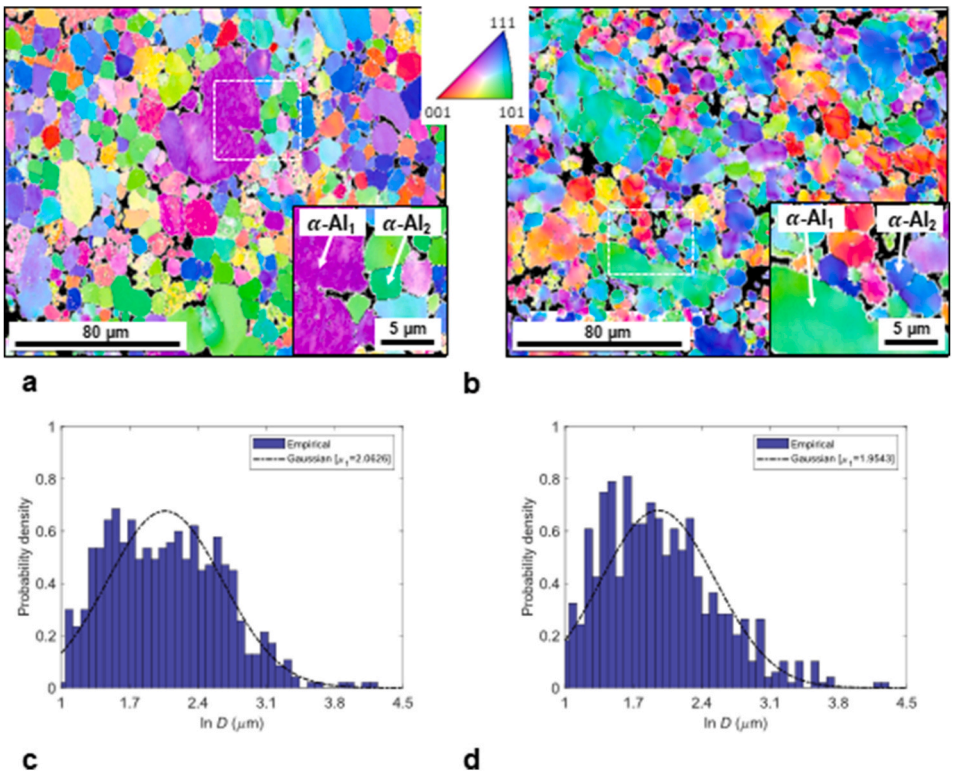

Fig. 6. EBSD Mapping of primary α-Al grains in specimens produced under (a,c) Baseline, and (b,d) Optimized conditions. Shown are IPF maps (a,b), and corresponding grain size distributions (c,d). Insets in (a) and (b) show enlarged images of the dashed regions. Fitted Gaussian functions, with expected value µ1, are shown as dashpot lines in (c,d).

natural logarithm (i.e. ln D). The two distributions are multimodal—an observation that is more pronounced in the Baseline distribution than in the Optimized distribution. In accordance with previous studies [27,28], a threshold size of 30 μm was used to distinguish primary α-Al_1 grains from primary α-Al_2 grains. Primary α-Al_1 grains are, on average, smaller in the Optimized condition (42.0 ± 13.8 μm) than in the Baseline condition (47.5 ± 14.0 μm). A similar trend is observed for primary α-Al_2 grains, with average values of 9.0 ± 5.4 μm and 8.0 ± 5.0 μm reported for the Baseline and Optimized conditions, respectively. Additionally, we can infer from the shape of the distributions that a more uniform grain structure is produced under Optimized conditions.

4. Discussion

4.1. Statistical analysis of tensile ductility

Here, the generalized extreme value (GEV) distribution is used to model the limiting distribution of tensile ductility for specimens produced under Baseline and Optimized conditions. A detailed description of the GEV distribution is provided in Ref. [29]. The cumulative distribution function of the GEV distribution is

$$G(x) = \exp\left\{ -\left[1+\xi\left(\frac{x-\mu}{\sigma}\right)\right]^{-1/\xi}\right\},\ 1+\xi\left(\frac{x-\mu}{\sigma}\right)>0 \quad (1)$$

where μ, σ, and ξ describe the location, scale, and shape of the distribution respectively. $G(x)$ is equivalent to the Gumbel, Fréchet, and Weibull functions when $\xi \to 0$, $\xi > 0$, and $\xi < 0$, respectively. The quantile function is obtained by inverting **(1)** for $G(X) = 1 - p$:

$$X = \mu - \frac{\sigma}{\xi}\left[1-\{-\log(1-p)\}^{-\xi}\right], \quad for\ \xi \neq 0,$$

$$X = \mu - \sigma\log\{-\log(1-p)\}, \quad for\ \xi = 0 \quad (2)$$

where X is the return level associated with a return period m and probability $p = 1/m$. It is important to note that equations (1) and (2) are defined for the case of maxima, not minima. To model minima, we use the substitution $x_i = -y_i$, where y_i denote our values of tensile ductility (small values of y_i now correspond to large values of x_i). Parameter estimates were obtained by maximum-likelihood estimation, with the sign correction $\tilde{\mu} = -\mu$. Parameter estimates and 95% confidence intervals are provided in Table 3. The change in plunger kinematics has little effect on the threshold value $\tilde{\mu}$. However, the tail behaviour of the two distributions is markedly different. For example, the negative shape parameter $\xi = -0.481$ implies that the Optimized distribution possesses a finite upper bound of $\sim -9.6\%$. Conversely, the positive shape parameter $\xi = 0.102$ suggests that the Baseline distribution is boundless; the return level plots in Fig. 7 exemplify this disparity. To demonstrate the practical implications of ξ, let us consider a hypothetical design criterion requiring a minimum ductility of 10%. From equation (2), we obtain scrap-rates of 12.5% and 5.7% for specimens produced under Baseline and Optimized conditions, respectively (i.e. $100/m$, for $X = -10\%$). Thus, by changing the kinematics of the plunger we have effectively halved the scrap rates in our imaginary foundry.

Table 3
GEV parameter estimates used to model the limiting distribution of tensile ductility for specimens produced under Baseline and Optimized conditions.

	ξ-mean	ξ– 95% Confidence intervals	σ	$\tilde{\mu}$
Baseline	0.102	[−0.070; 0.275]	1.06	12.3
Optimized	−0.481	[−0.589; −0.373]	1.26	12.2

4.2. Source of variability in tensile ductility

Previous studies [5–7] have shown that the tensile fracture properties of aluminium alloy die-castings depend on the maximum defect size, with other factors (such as defect morphology, size distribution, and volume fraction) of secondary importance. Fig. 8 plots the tensile ductility of a specimen against the size of the largest defect observed on its fracture surface; defects in Fig. 8 are classified as either pores or inclusions. A power-law relationship of the form $y = ax^b$, was fitted to the overall data, as shown by the dashpot line in Fig. 8. The power-law accurately captures the behaviour of the empirical data (coefficient of determination $R^2 = 0.858$) when the constants a and b take values of 4.461 and −0.525, respectively. From Fig. 8, it seems that inclusions ∼ 0.75 mm in diameter have a similar effect on the tensile ductility as pores in the range of 0.90 ∼ 1.50 mm. However, this is likely due to the location of these defects with respect to the specimen free surface, as opposed to the potency of the defects themselves—while pores typically congregate in the central core, non-metallic inclusions are often observed near to the specimen free surface. Strain localises more rapidly at surface defects and sub-surface defects compared to internal defects of an equivalent size [30]. Few oxides were observed on the fracture surfaces of the tensile specimens, and when they were observed they were negligibly small in size; no other abnormalities were observed on the fracture surface of the examined specimens. Based on these considerations, we infer that the observed scatter in tensile ductility is caused by variations in the size of large pores and non-metallic inclusions, the origins of which we now discuss.

4.3. Origin of non-metallic inclusions

Oil-based lubricants are often applied to the plunger tip to prevent wear and seizure. The tribological performance of such lubricants rely on the formation of a low-viscosity film between the contacting surfaces. When liquid metal enters the shot chamber, it reacts with organic compounds contained in the plunger lubricant to produce gaseous phases [31] and a carbonaceous residue [32]—this pyrolysis presents itself as a flame emerging from the pouring hole. This residue may be entrained into the liquid during solidification processing, materializing as non-metallic inclusions in the residual microstructure. Variations in inclusion size may then depend on the rate of build-up, and the viscous forces leading to detachment and breakage.

EDX analysis (see insert of Fig. 5(b)) reveals that these inclusions typically contain C, Na, S, Cl, K, and Ca. Due to its low atomic mass, the presence of C does not substantiate the pyrolysis hypothesis; C is also a common contaminant in electron microscopes. Let us, therefore, turn our attention to the heavier elements: Na, S, Cl, K and Ca. Petrochemical or synthetic based additives are often added to base stocks to impart additional properties to the lubricant. Extreme pressure additives enhance lubricity in high-pressure environments, and often contain compounds of S or Cl [33]. Other additives, such as surfactants and thickeners, are also used in commercial lubricants, often containing compounds of Na, K and Ca [34]. The presence of Na, S, Cl, K, and Ca in the observed inclusions is therefore consistent with the chemical constituents of commercial plunger lubricants. To test the pyrolysis hypothesis, filling tests were performed by allowing the melt to solidify in the shot chamber with the plunger at rest (see Appendix). Large films, that closely resemble the non-metallic inclusions shown in Fig. 5(b), were identified on the surface of the solidified billets (Fig. A1). Hence, we propose that these non-metallic inclusions form during the pyrolysis of commercial plunger lubricants in the shot chamber. One might argue that the aforementioned elements are also found in commercial foundry fluxes; however, no flux was used in our experiments.

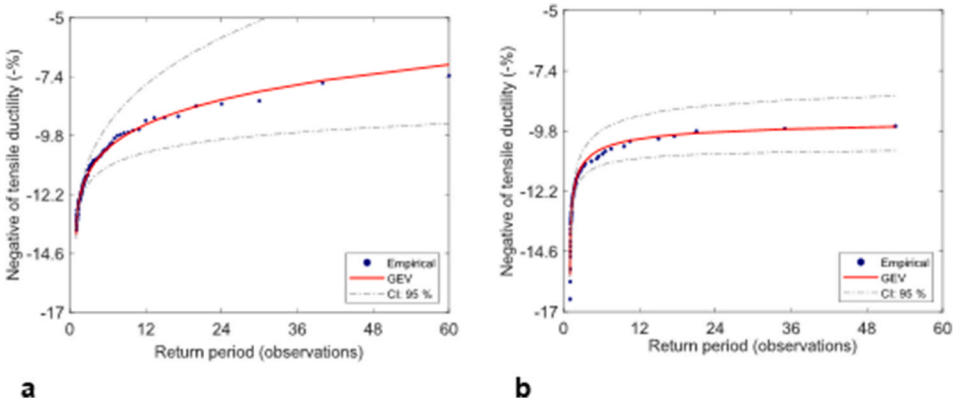

Fig. 7. Predicted values (GEV) of tensile ductility for specimens produced under (a) Baseline, and (b) Optimized, conditions. The GEV curve was calculated from equation (2) for $x_i = -y_i$, where y_i denote our values of tensile ductility (hence units of - %). Its magnitude thus represents an upper limit to the minimum tensile ductility expected in a group of m specimens (abscissa). For comparison, experimental data points x_i are plotted in ascending order. Note that only unique values of x_i are considered (hence the upper limit of 60 observations). 95% confidence intervals are shown as dashpot lines (CI: 95%).

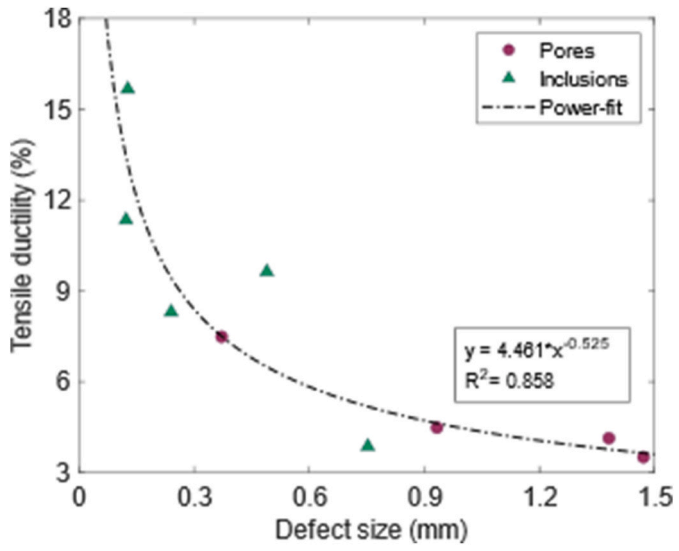

Fig. 8. Tensile ductility vs. maximum defect size (D). A power-law relationship is fitted to the overall data. R^2 denotes the coefficient of determination.

4.4. Origin of porosity

Previously we found that a change in plunger kinematics may lead to a decrease in the maximum pore size; however, the average pore size remained unchanged. We also related the observed scatter in tensile ductility to variations in the size of these large pores. Fewer oxides accumulate in the casting under Optimized conditions, due to a calmer free surface during fluid flow [22]. However, no relationship was observed between the tensile ductility of a specimen and its position in the die. Furthermore, the average gas content is lower in the Optimized condition than in the Baseline condition, due to reduced air entrapment in the shot chamber [22]. Although an increase in gas content would certainly expedite pore growth, it is unlikely that a small difference would have a significant effect. Moreover, one would expect the average pore size to also increase following an increase in the average gas content.

An alternative explanation lies in the response of the semi-solid alloy to shear deformation. During the intensification stage, a pressure of 30 $\sim$ 100 MPa [1] is applied to the solidifying alloy to compress gaseous phases and to assist in the feeding of shrinkage strains. Previous studies [35–38] have shown that metallic alloys at 60 $\sim$ 95% solid deform as near-cohesionless granular materials, exhibiting phenomena such as Reynold's dilatancy and granular rearrangement. Under compression, a pore will either contract or dilate depending on the solid fraction at which deformation occurs [35,36]. At low solid fractions, grains are able to move towards one another, applying an external pressure on the pore, driving closure [36]. At high solid fractions, grains are so densely packed that grain rearrangement leads to shear-induced dilation and pore growth [36]. Kareh et al. [35] report a volumetric increase of $\sim$ 622% for a pore in an Al–Cu alloy deformed at 93% solid. The maximum volumetric strain increases with the solid fraction at which deformation occurs [35,36]. Furthermore, the melt temperature at the end of die filling is 30 °C higher in the Optimized condition compared to the Baseline condition [22]. Thus, the change in plunger kinematics from Baseline to Optimized will lead to a decrease in the maximum volumetric strain encountered during semi-solid deformation. Dilatational strains are highly localised and time variant, and may lead to the formation of a new pore, or the sudden expansion of an existing pore [35,36]. This dependency on the local grain structure may explain the seemingly random nature of pore formation in the HPDC process. This supposition is further supported by the grain size distributions in Fig. 6(c and d): a more uniform grain structure is produced under Optimized conditions, which is expected to result in a more homogeneous strain field, reducing scatter in pore size.

5. Conclusions

1. Scatter in tensile ductility is related to the size of large pores and non-metallic inclusions, for specimens produced under the observed conditions. A power-law relationship is established between the tensile ductility and the size of the largest defect on the fracture surface, which is irrespective of defect type.
2. We propose that these non-metallic inclusions form during the pyrolysis of commercial plunger lubricants in the shot chamber. This hypothesis is based on the chemical constituents of the inclusions, and is substantiated by shot chamber filling tests.
3. Scatter in tensile ductility is greatly reduced under Optimized conditions, due to a decrease in the maximum pore size from 1.32 mm to 0.37 mm. Our findings suggest that these large pores derive from dilatational strains introduced during semi-solid deformation. The apparent randomness of pore formation is thus attributed to the heterogeneous nature of the semi-solid network. Indeed, a more uniform grain structure is produced under Optimized conditions, which is expected to result in a more homogeneous strain field, reducing scatter in pore size.

Data availability

The raw/processed data required to reproduce these findings cannot be shared at this time due to legal or ethical reasons.

CRediT authorship contribution statement

Ewan Lordan: Conceptualization, Methodology, Validation, Formal

analysis, Investigation, Writing – original draft, Writing – review & editing, Visualization. **Yijie Zhang:** Conceptualization, Methodology, Validation, Investigation, Writing – review & editing. **Kun Dou:** Conceptualization, Methodology, Software, Formal analysis, Writing – review & editing, Visualization. **Alain Jacot:** Conceptualization, Methodology, Software, Writing – review & editing, Supervision, Project administration. **Chrysoula Tzileroglou:** Methodology, Investigation, Visualization. **Paul Blake:** Supervision, Project administration, Funding acquisition. **Zhongyun Fan:** Conceptualization, Supervision, Funding acquisition.

Declaration of competing interest

The authors declare that they have no known competing financial interests or personal relationships that could have appeared to influence the work reported in this paper.

Acknowledgments

This work was supported by the Engineering and Physical Sciences Research Council and Jaguar Land Rover Ltd. [project reference 2043200].

Appendix

To test the pyrolysis hypothesis, filling tests were performed by allowing the liquid to solidify in the shot chamber with the plunger at rest (Fig. A1). Fig. A1(b) shows a photograph of one of these filling test samples, with a close-up provided in Fig. A1(c). In Fig. A1(b), the location of the pouring hole is referred to by the phrase 'inlet'; in the experiment, the plunger was in contact with the left-hand surface of the billet. As shown in Fig. A1(c), large films are observed on the surface of the billet. Furthermore, these films closely resemble the non-metallic inclusions shown in Fig. A1(b). Based on these results, it seems plausible that the aforementioned non-metallic inclusions form during the pyrolysis of commercial plunger lubricants. One might argue that the aforementioned elements are also found in commercial foundry fluxes; however, no flux was used during our experiments.

To ensure our findings are indeed representative of industry, fatigue specimens were machined from automotive components produced by HPDC. Various alloys were studied for samples produced by different suppliers. Crack initiating defects were identified via SEM fractography. Critical casting defects were identified as porosity, oxide films, and non-metallic inclusions—a representative BSE micrograph is shown in Fig. A1(a). Although, the Baseline process appears to be representative of industrial practice, oxides are more prominent in the automotive castings compared to Baseline samples. This is attributed to the increased geometric complexity of automotive components, and the use of sub-optimal melt handling procedures in commercial foundries (it is more difficult to control melt cleanliness in a commercial foundry than it is in a laboratory environment). As the suppliers cannot disclose their practices, we are unable to dismiss the use of foundry flux during casting.

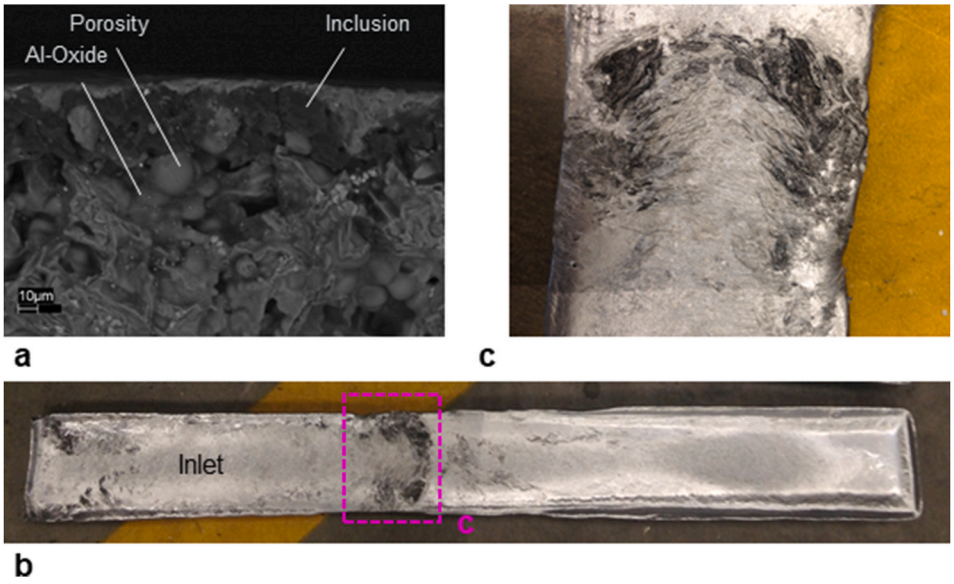

Fig. A1. Origin of non-metallic inclusions. (a) Representative micrograph of a non-metallic inclusion observed on the fracture surface of a fatigue specimen machined from an automotive component. (b) Photograph of a shot chamber filling test sample (inlet refers to the pouring hole). (c) Close up of the dashed region in (b).

References

[1] X.P. Niu, K.K. Tong, B.H. Hu, I. Pinwill, Cavity pressure sensor study of the gate freezing behaviour in aluminium high pressure die casting, Int. J. Cast. Met. Res. 11 (1998) 105–112, https://doi.org/10.1080/13640461.1998.11819264.

[2] Y. Zhang, J.B. Patel, J. Lazaro-Nebreda, Z. Fan, Improved defect control and mechanical property variation in high-pressure die casting of A380 alloy by high shear melt conditioning, J. Occup. Med. 70 (2018) 2726–2730, https://doi.org/10.1007/s11837-018-3005-y.

[3] S. Ji, H. Yang, D. Watson, Z. Fan, Weibull analysis for the repeatability of die castings made by an Al-Mg-Si-Mn alloy, Light Met. (2016) 681–685, https://doi.org/10.1007/978-3-319-48251-4_114.

[4] X. Dong, X. Zhu, S. Ji, Effect of super vacuum assisted high pressure die casting on the repeatability of mechanical properties of Al-Si-Mg-Mn die-cast alloys, J. Mater. Process. Technol. 266 (2019) 105–113, https://doi.org/10.1016/j.jmatprotec.2018.10.030.

[5] J.P. Weiler, J.T. Wood, R.J. Klassen, E. Maire, R. Berkmortel, G. Wang, Relationship between internal porosity and fracture strength of die-cast magnesium AM60B alloy, Mater. Sci. Eng., A 395 (2005) 315–322, https://doi.org/10.1016/j.msea.2004.12.042.

[6] J.P. Weiler, J.T. Wood, Modeling fracture properties in a die-cast AM60B magnesium alloy I—analytical failure model, Mater. Sci. Eng., A 527 (2009) 25–31, https://doi.org/10.1016/j.msea.2009.08.060.

[7] E. Lordan, J. Lazaro-Nebreda, Y. Zhang, K. Dou, P. Blake, Z. Fan, On the relationship between internal porosity and the tensile ductility of aluminium alloy die-castings, Mater. Sci. Eng. 778 (2020) 139107, https://doi.org/10.1016/j.msea.2020.139107.

[8] E. Lordan, J. Lazaro-Nebreda, Y. Zhang, Z. Fan, Effective degassing for reduced variability in high-pressure die casting performance, J. Occup. Med. 71 (2019) 824–830, https://doi.org/10.1007/s11837-018-3186-4.
[9] C. Tian, J. Law, J. van der Touw, M. Murray, J.-Y. Yao, D. Graham, D. St John, Effect of melt cleanliness on the formation of porosity defects in automotive aluminium high pressure die castings, J. Mater. Process. Technol. 122 (2002) 82–93, https://doi.org/10.1016/S0924-0136(01)01229-8.
[10] G. Timelli, A. Fabrizi, The effects of microstructure heterogeneities and casting defects on the mechanical properties of high-pressure die-cast AlSi9Cu3(Fe) alloys, Metall. Mater. Trans. 45 (2014) 5486–5498, https://doi.org/10.1007/s11661-014-2515-7.
[11] S. Ferraro, G. Timelli, Influence of sludge particles on the tensile properties of die-cast secondary aluminum alloys, Metall. Mater. Trans. B 46 (2015) 1022–1034, https://doi.org/10.1007/s11663-014-0260-3.
[12] H. Yang, S. Ji, D. Watson, Z. Fan, Repeatability of tensile properties in high pressure die-castings of an Al-Mg-Si-Mn alloy, Met. Mater. Int. 21 (2015) 936–943, https://doi.org/10.1007/s12540-015-5108-0.
[13] X. Li, S.M. Xiong, Z. Guo, Improved mechanical properties in vacuum-assist high-pressure die casting of AZ91D alloy, J. Mater. Process. Technol. 231 (2016) 1–7, https://doi.org/10.1016/j.jmatprotec.2015.12.005.
[14] H. Gjestland, S. Sannes, J. Svalestuen, H. Westengen, Optimizing the magnesium die casting process to achieve reliability in automotive applications, SAE Trans. 114 (2005) 67–73. https://www.jstor.org/stable/44718874?seq=1.
[15] X. Li, S.M. Xiong, Z. Guo, On the porosity induced by externally solidified crystals in high-pressure die-cast of AM60B alloy and its effect on crack initiation and propagation, Mater. Sci. Eng., A 633 (2015) 35–41, https://doi.org/10.1016/j.msea.2015.02.078.
[16] S. Ji, W. Yang, F. Gao, D. Watson, Z. Fan, Effect of iron on the microstructure and mechanical property of Al–Mg–Si–Mn and Al–Mg–Si diecast alloys, Mater. Sci. Eng., A 564 (2013) 130–139, https://doi.org/10.1016/j.msea.2012.11.095.
[17] K. Dou, E. Lordan, Y.J. Zhang, A. Jacot, Z.Y. Fan, Numerical simulation of fluid flow, solidification and defects in high pressure die casting (HPDC) process, IOP Conf. Ser. Mater. Sci. Eng. 529 (2019), 012058, https://doi.org/10.1088/1757-899X/529/1/012058.
[18] M. Saeedipour, S. Schneiderbauer, S. Pirker, S. Bozorgi, A numerical and experimental study of flow behaviour in high pressure die casting, Magnesium Technol (2014) 185–190, https://doi.org/10.1007/978-3-319-48231-6_37.
[19] D.R. Gunasegaram, M. Givord, R.G. O'Donnell, B.R. Finnin, Improvements engineered in UTS and elongation of aluminum alloy high pressure die castings through the alteration of runner geometry and plunger velocity, Mater. Sci. Eng., A 559 (2013) 276–286, https://doi.org/10.1016/j.msea.2012.08.098.
[20] X. Li, W. Yu, J. Wang, S. Xiong, Influence of melt flow in the gating system on microstructure and mechanical properties of high pressure die casting AZ91D magnesium alloy, Mater. Sci. Eng., A 736 (2018) 219–227, https://doi.org/10.1016/j.msea.2018.08.090.
[21] K. Dou, E. Lordan, Y.J. Zhang, A. Jacot, Z.Y. Fan, A complete computer aided engineering (CAE) modelling and optimization of high pressure die casting (HPDC) process, J. Manuf. Process. 60 (2020) 435–446, https://doi.org/10.1016/j.jmapro.2020.10.062.
[22] K. Dou, E. Lordan, Y. Zhang, A. Jacot, Z. Fan, Improvement of Mechanical Properties for Aluminium Alloy in High Pressure Die Casting (HPDC) Process Combining Experimental and Modelling Approach, 2020 manuscript submitted for publication.
[23] D.G. Eskin, I. Tzanakis, F. Wang, G.S.B. Lebon, T. Subroto, K. Pericleous, J. Mi, Fundamental studies of ultrasonic melt processing, Ultrason. Sonochem. 52 (2019) 455–467, https://doi.org/10.1016/j.ultsonch.2018.12.028.
[24] ASTM Committee, Test methods for tension testing of metallic materials, ASTM international. http://www.astm.org/cgi-bin/resolver.cgi?E8E8M-16AE1 (accessed September 10, 2020).
[25] J. Campbell, Castings, second ed., Butterworth-Heinemann, 2002.
[26] R.B. Bergmann, A. Bill, On the origin of logarithmic-normal distributions: an analytical derivation, and its application to nucleation and growth processes, J. Cryst. Growth 310 (2008) 3135–3138, https://doi.org/10.1016/j.jcrysgro.2008.03.034.
[27] S. Otarawanna, C.M. Gourlay, H.I. Laukli, A.K. Dahle, Microstructure formation in AlSi4MgMn and AlMg5Si2Mn high-pressure die castings, Metall. Mater. Trans. 40 (2009) 1645–1659, https://doi.org/10.1007/s11661-009-9841-1.
[28] S. Otarawanna, C.M. Gourlay, H.I. Laukli, A.K. Dahle, Agglomeration and bending of equiaxed crystals during solidification of hypoeutectic Al and Mg alloys, Acta Mater. 58 (2010) 261–271, https://doi.org/10.1016/j.actamat.2009.09.002.
[29] S. Coles, An Introduction to Statistical Modeling of Extreme Values, Springer, 2001, https://doi.org/10.1007/978-1-4471-3675-0.
[30] A. Borbély, H. Mughrabi, G. Eisenmeier, H.W. Höppel, A finite element modelling study of strain localization in the vicinity of near-surface cavities as a cause of subsurface fatigue crack initiation, Int. J. Fract. 115 (2002) 227–232, https://doi.org/10.1023/A:1016350528652.
[31] L. Wang, P. Turnley, G. Savage, Gas content in high pressure die castings, J. Mater. Process. Technol. 211 (2011) 1510–1515, https://doi.org/10.1016/j.jmatprotec.2011.03.024.
[32] Tribo-chemie GmbH, The thermal reaction of different plunger lubricants and its influence on casting quality. https://tribochemie.de/images/media/downloads/EN/plungerlubricant.pdf (accessed August 20, 2020)..
[33] T. Mang, W. Dresel, Lubricants and Lubrication, John Wiley & Sons, 2007.
[34] ATC Europe, Lubricant Additives: use and Benefits, 2016. https://www.atc-europe.org/public/Document%20118%20-%20Lubricant%20Additives%20Use%20and%20Benefits.pdf. (Accessed 20 August 2020).
[35] K.M. Kareh, P.D. Lee, R.C. Atwood, T. Connolley, C.M. Gourlay, Revealing the micromechanisms behind semi-solid metal deformation with time-resolved X-ray tomography, Nat. Commun. 5 (2014) 4464, https://doi.org/10.1038/ncomms5464.
[36] K.M. Kareh, P.D. Lee, R.C. Atwood, T. Connolley, C.M. Gourlay, Pore behaviour during semi-solid alloy compression: insights into defect creation under pressure, Scripta Mater. 89 (2014) 73–76, https://doi.org/10.1016/j.scriptamat.2014.06.033.
[37] C.M. Gourlay, A.K. Dahle, Dilatant shear bands in solidifying metals, Nature (Paris) 445 (2007) 70–73, https://doi.org/10.1038/nature05426.
[38] T.C. Su, C. O'Sullivan, T. Nagira, H. Yasuda, C.M. Gourlay, Semi-solid deformation of Al-Cu alloys: a quantitative comparison between real-time imaging and coupled LBM-DEM simulations, Acta Mater. 163 (2019) 208–225, https://doi.org/10.1016/j.actamat.2018.10.006.